



Three-dimensional finite element analyses of reinforced concrete columns

Minho Kwon^a, Enrico Spacone^{b,*}

^a Department of Civil Engineering, Kyungpook National University, 1370 Sankyuk-dong Puk-gu, Daegu 702-701, South Korea

^b Department of Civil, Environmental and Architectural Engineering, University of Colorado, Campus Box 428, Boulder, CO 80309-0428, USA

Received 25 September 2000; accepted 16 August 2001

Abstract

A recently developed three-dimensional concrete law is used for the analysis of concrete specimens and reinforced concrete columns subjected to different load patterns. The hypoelastic, orthotropic concrete constitutive model includes coupling between the deviatoric and volumetric stresses, works with both proportional and non-proportional loads and is implemented as a strain driven module. The finite element (FE) implementation is based on the smeared crack approach with rotating cracks parallel to the principal strain directions. The concrete model is validated through correlation studies with: (a) experimental tests on concrete cylinders confined by different mechanisms, including steel and fiber reinforced polymer jackets; (b) experimental results on three reinforced concrete columns tested at the University of California, San Diego. The correlations are overall very good, and the FE responses capture all the main phenomena observed in the experimental tests. © 2002 Published by Elsevier Science Ltd.

Keywords: Constitutive model; Finite element analysis; Concrete; Hypoelastic model; Orthotropic model; Equivalent uniaxial strain; Reinforced concrete columns; Steel jackets; Fiber reinforced polymer jackets

1. Introduction

Finite element (FE) analyses are performed to gain a better understanding of the behavior and characteristics of reinforced concrete (RC) structures under a variety of loading and boundary conditions. While simplified analyses that use either beam elements or two-dimensional finite elements are quite useful, only three-dimensional analyses can fully represent all the aspects of the response of concrete structures.

Three-dimensional analyses of RC structures require the availability of three-dimensional concrete laws that can describe the main features of the nonlinear concrete response under triaxial states of stress, such as com-

pression crushing, tensile cracking, increased strength and ductility under large confining stresses, etc. All these phenomena are of primary importance for the accurate description of the physical behavior of RC structures, such as RC columns with different shear reinforcement subjected to large lateral deformations. In some special situations, only a three-dimensional analysis can provide certain response information of interest to the designer that the other methods cannot provide.

The implementation of concrete laws in a FE environment adds to the complexity of the task, because of discretization errors and because concrete is a highly discontinuous, non-homogeneous material, while the FE discretization tends to treat it as a continuous medium. In particular, cracking is a discontinuous phenomenon that is typically treated with two major approaches; discrete and smeared crack. The concept of the discrete crack approach is well matched with the nature of the physical cracks; however, the crack regions have to be

* Corresponding author. Tel.: +1-303-492-7607; fax: +1-303-492-7317.

E-mail address: spacone@colorado.edu (E. Spacone).

pre-defined or remeshing is required. The smeared crack approach better fits the FE philosophy, but it may lead to overestimation of the shear strength of structural members. In turn, smeared cracks can be fixed or rotating.

As for the steel reinforcement in RC structural members, it is modeled by either discrete bar elements, it is embedded in solid finite elements or it is smeared over the volume of the finite element. According to Darwin [1], the different modeling schemes for the steel reinforcement do not have a significant impact on the results.

This study focuses on the application of a three-dimensional concrete constitutive law recently developed by Balan et al. [2] to the study of concrete cylinders under different confinement mechanisms and to the analyses of RC columns experimentally tested at the University of California, San Diego. The main scope of this paper is to validate the proposed model, to outline its characteristics and to point to its shortcomings, whose understanding is central to a critical evaluation of the results of the FE analyses.

$$\mathbf{C}_0 = \frac{1}{\Omega} \begin{bmatrix} E_1(1 - \nu_{23}\nu_{32}) & E_1(\nu_{21} + \nu_{23}\nu_{31}) & E_1(\nu_{31} + \nu_{21}\nu_{32}) & 0 & 0 & 0 \\ E_2(\nu_{12} + \nu_{13}\nu_{32}) & E_2(1 - \nu_{13}\nu_{31}) & E_2(\nu_{32} + \nu_{12}\nu_{31}) & 0 & 0 & 0 \\ E_3(\nu_{13} + \nu_{12}\nu_{23}) & E_3(\nu_{23} + \nu_{13}\nu_{21}) & E_3(1 - \nu_{12}\nu_{21}) & 0 & 0 & 0 \\ 0 & 0 & 0 & G_{12}\Omega & 0 & 0 \\ 0 & 0 & 0 & 0 & G_{23}\Omega & 0 \\ 0 & 0 & 0 & 0 & 0 & G_{31}\Omega \end{bmatrix} \quad (2)$$

2. Material models

A three-dimensional constitutive model for the concrete and a uniaxial steel model are required to analyze the RC sub-assemblages discussed in this paper. In the last two decades, numerous models have been developed for describing concrete behavior under various stress states. Many concrete constitutive models are not economically viable for large-scale analyses of concrete structures because of the complexity in both the non-linear stress–strain relation and in the geometry of structures. Necessary features of a concrete model applicable to practical problems should be on one hand the accurate simulation of the actual concrete behavior, and on the other the simplicity in formulation and the efficient implementation in a robust and stable non-linear algorithm. As emphasized by Gerstle [3], the simplicity of a constitutive model should appeal to professional engineers. A good compromise between simplicity and accuracy is accomplished in this study by a three-dimensional hypoelastic model recently developed by Balan et al. [2]. The model can describe the cyclic response of concrete under proportional and non-proportional loading.

2.1. Triaxial concrete stress–strain model

The main features of the concrete model proposed by Balan et al. [2] are presented in this section, with emphasis on the enhancements to the original model and on the numerical implementation issues. The model stems from a hypoelasticity approach based on non-linear elasticity and has stress-induced orthotropy. The model captures shear dilatation, non-proportional loading and the cyclic response of concrete. The law is based on the equivalent uniaxial strain concept introduced by Darwin and Pecknold [4]. The material orthotropic axes are assumed parallel to the principal stress axes. The principal stress axes are not coaxial with the principal strain axes.

The incremental stress–strain relation of concrete with respect to the orthotropic axes is

$$d\boldsymbol{\sigma} = \mathbf{C}_0 d\boldsymbol{\varepsilon} \quad (1)$$

where $d\boldsymbol{\sigma}$ and $d\boldsymbol{\varepsilon}$ are the stress and strain increments, respectively, and \mathbf{C}_0 is the following material matrix [2]

where: ν_{ij} is the transverse strain ratio for strain in j -direction caused by stress in i -direction ($i, j = 1, 2, 3$), $\Omega = 1 - \nu_{21}\nu_{12} - \nu_{31}\nu_{13} - \nu_{32}\nu_{23} - \nu_{12}\nu_{23}\nu_{31} - \nu_{21}\nu_{32}\nu_{13}$, E_i is material modulus in i -direction of orthotropy ($i = 1, 2, 3$), G_{ij} is shear modulus in i - j plane.

Asymmetric crack opening leads to the use of asymmetric Poisson's ratios. Poisson's ratios are derived from the symmetry requirement of the material matrix. Because the shear moduli G_{ij} ($i, j = 1, 2, 3$) must be invariant under an arbitrary coordinate transformation, it can be shown [23] that the shear moduli are

$$G_{ij} = \frac{E_i E_j}{E_i(1 + \nu_{ij}) + E_j(1 + \nu_{ji})} \quad (3)$$

Using the equivalent uniaxial strain concept proposed by Darwin and Pecknold [4], the three-dimensional constitutive relation can be uncoupled into three distinct uniaxial stress–strain relations. The equivalent uniaxial strain is a fictitious strain with no precise material meaning. For given principal stresses σ_{p_i} , the equivalent uniaxial strains ε_{w_i} are the strains that would induce the same stresses on the equivalent uniaxial stress–strain curves. The material parameters that define the equivalent

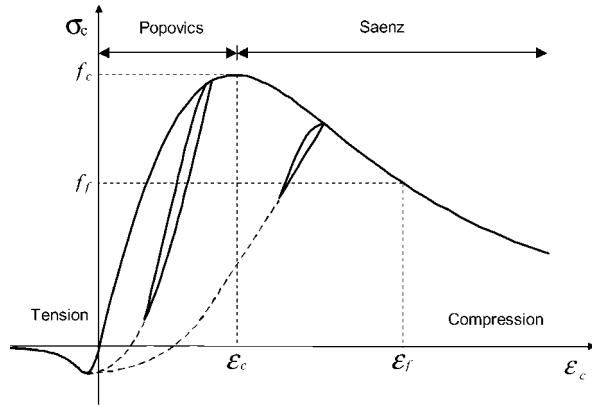


Fig. 1. Popovics–Saenz curve (proposed by Balan et al. [2]).

lent uniaxial stress–strain curves depend on the current stress ratio, as discussed later in the paper. The equivalent uniaxial strains are typically derived from the incremental law $d\varepsilon_{ui} = d\sigma_{pi}/E_i$ ($i = 1, 2, 3$), where E_i is the material modulus. In this study, the total secant modulus is used. The total equivalent uniaxial strain is defined as the integral of the incremental strains $d\varepsilon_{ui}$. In the numerical implementation of the incremental law, the infinitesimal increments $d\varepsilon$, $d\sigma$ become finite increments $\Delta\varepsilon$, $\Delta\sigma$.

A uniaxial concrete law is required to obtain the stress corresponding to ε_{ui} . Kwon [5] proposes to use Popovics' [6] curve up to the peak compressive stress and Saenz' [7] curve after the peak. The law is shown in Fig. 1 and is defined by a single equation

$$\sigma = f_c \frac{K(\varepsilon/\varepsilon_c)}{1 + A(\varepsilon/\varepsilon_c) + B(\varepsilon/\varepsilon_c)^2 + C(\varepsilon/\varepsilon_c)^3 + D(\varepsilon/\varepsilon_c)^r} \quad (4)$$

where, $K = E_0(\varepsilon_c/f_c)$; $K_e = \varepsilon_f/\varepsilon_c$; $K_\sigma = f_c/f_t$; $r = K/(K - 1)$;

Popovics' Curve if $(\varepsilon/\varepsilon_c) < 1$

$$A = C + K - 2; \quad B = 1 - 2C;$$

$$C = K \frac{(K_\sigma - 1)}{(K_e - 1)^2} - \frac{1}{K_e}; \quad D = 0$$

Saenz' Curve if $(\varepsilon/\varepsilon_c) \geq 1$

$$A = B = C = 0; \quad D = K - 1$$

E_c is initial modulus of elasticity, ε_u , uniaxial strain, f_c , material strength, ε_c , uniaxial strain corresponding to f_c and f_t , ε_f , control point on the descending branch of the stress–strain curve.

Equations similar to Eq. (4) are defined in tension, with initial stiffness E_0 and peak point ε_t , f_t .

2.1.1. Ultimate surface

The stress–strain curves defined by Eq. (4) are functions of the peak stresses f_{ci} and the corresponding strains ε_{ci} , where the subscript i indicates the three principal stress directions (i.e., $i = 1, 2, 3$). f_{ci} and ε_{ci} are defined by two ultimate surfaces in the principal stress space and in the equivalent uniaxial strain space, respectively.

The ultimate stress surface defines the ultimate stress values f_{c1} , f_{c2} , f_{c3} for a given principal stress ratio $\sigma_{p1}/\sigma_{p2}/\sigma_{p3}$. These are not failure points, but rather combinations of maximum stress values (ultimate stresses). The ultimate stress surface of concrete used in this work is a modification of the five-parameter failure surface of Willam and Warnke [8]. It is a combination of the traditional Rankine criterion of maximum tensile strength and the Mohr–Coulomb criterion of shear strength. The modified surface is described by

$$\tau_0^2 + A \left(\frac{\tau_0}{\sqrt{2}} r(e, \varphi) + \sigma_0 \right) + B = 0 \quad (5)$$

where $r(e, \varphi)$ is the polar radius as defined by Menetrey and Willam [9]:

$$r(e, \varphi) = \frac{a\eta^2 + b^2}{a\eta + b\sqrt{a(\eta^2 - 1) + b^2}} \quad (6)$$

and

$$A = \frac{f_c^2 - f_t^2}{9f_c} (2 + \alpha); \quad B = -\frac{2f_c f_t}{9}$$

$\alpha(f_t/f_c)$ is material brittleness, f_c , f_t are uniaxial compression and tensile strength, respectively.

$$a = 1 - e^2; \quad b = 2e - 1; \quad \eta = 2 \cos(\varphi),$$

$$\varphi = \frac{1}{3} \arccos[(3\sqrt{3}/2)(J_3/(J_2)^{3/2})]$$

is the Lode angle of orientation of the stress-point in the deviatoric plane with J_2 and J_3 being the second and third invariant of the deviatoric stress tensor. e is the eccentricity that defines the out of roundness of the deviatoric section of the failure surface. For $0.5 \leq e \leq 1.0$ it describes a smooth convex (elliptical) curve. Menetrey and Willam [9] suggested $e = 0.52$ for biaxial loading based on a brittleness $\alpha = 0.1$. A series of tests summarized by the Comité Euro-Internation du Béton [10] shows that the eccentricity for concrete should be $0.5 \leq e \leq 0.6$. Balan et al. [2] propose a unique equation for e , expressed in terms of the material brittleness α :

$$e = \frac{2 + \alpha}{4 - \alpha} \quad (7)$$

Eq. (7) indicates that the brittleness should be larger than zero to keep the shape of the deviatoric section smooth, that is, the tensile strength has to be larger than

zero. When the brittleness is equal to one, the eccentricity becomes unity and the deviatoric section becomes a circle, which is a suitable failure surface for metals such as steel. When the brittleness is equal to 0.1, the eccentricity becomes 0.538, which is close to the value suggested by Menetrey and Willam [9]. To capture failure at or near hydrostatic loading, cap surfaces are introduced in the failure surface. These curves are functions of the hydrostatic stress and are defined in Ref. [2].

2.1.2. Poisson's ratios

The following expression is proposed by Balan et al. [2] to define the transverse strain ratios v_{ij}

$$v_{ij} = \sqrt{v_{ui}v_{uj} \frac{E_i}{E_j}} \quad (8)$$

where v_{ui} is the uniaxial transverse strain ratio in the direction i .

The above definition of v_{ui} satisfies the symmetry of C_0 in Eq. (2). The following expression is used to define v_{ui} :

$$v_{ui} = v_0 \left[1 + \frac{1}{K_v} \left\{ A_i \left(\frac{\varepsilon_{ui}}{\varepsilon_{ci}} \right) + B_i \left(\frac{\varepsilon_{ui}}{\varepsilon_{ci}} \right)^2 + C_i \left(\frac{\varepsilon_{ui}}{\varepsilon_{ci}} \right)^3 \right\} \right] \quad (9)$$

where v_0 is the initial Poisson's ratio, and

$$K = \frac{1}{2v_0}; \quad K_\varepsilon = \frac{\varepsilon_f}{\varepsilon_c}; \quad K_\sigma = \frac{f_c}{f_t}; \quad K_v = E_0 \frac{\varepsilon_c}{f_c}$$

$$A = C + K - 2; \quad B = 1 - 2C; \quad C = K \frac{(K_\sigma - 1)}{(K_\varepsilon - 1)^2} - \frac{1}{K_\varepsilon}$$

2.1.3. Confinement effects

The point (ε_f, f_t) , on the descending branch of the uniaxial stress–strain curve of Fig. 1 must be defined to complete the description of the uniaxial law. The concrete post-peak behavior highly depends on the test conditions. Increasing confinement stresses enhance the concrete strength and ductility, with a transition from brittle to ductile failure as the lateral confinement increases. The following empirical equation is introduced by Balan et al. [2] to capture this point based on the confined test results of Smith et al. [11]

$$f_t = \frac{f_{ci}f_c}{(5f_c - f_{ci})} \leq 1.4 \quad (10)$$

where f_c is the uniaxial compressive strength of concrete and f_{ci} is the ultimate strength in the orthotropic direction i determined from the failure surface.

2.1.4. Pure shear and simple shear tests

It has been observed that a concrete specimen loaded in a deviatoric stress plane exhibits volumetric changes. The original hypoelastic model proposal by Balan et al. [2] cannot describe such a response, because the normal and shear responses are uncoupled. Hence, the original model cannot correctly describe simple shear (only shear strains applied) and pure shear (only shear stresses applied) loading cases. This shortcoming has been corrected in the current version of the model. Following the definition of the coupling modulus proposed by Gerstle [12], an additional term containing the octahedral stress is added to the definition of the volumetric stress.

$$\sigma_{\text{vol}} = \frac{\sigma_1 + \sigma_2 + \sigma_3}{3} - 1.4142\beta\tau_{\text{oc}} \quad (11)$$

where $\beta = \tau_o/\tau_{\text{oc}}$, τ_o is the octahedral shear stress and τ_{oc} is the ultimate octahedral shear stress. $\tau_{\text{oc}} = 2G_0\gamma_o$ is the linear elastic octahedral shear stress, G_0 is the initial shear modulus and γ_o is the linear elastic octahedral shear strain. The additional term represents the volumetric stress induced by the deviatoric stress. In the equivalent strain space, a similar volumetric strain is defined.

Pure shear conditions are obtained in a pure torsion loading test under stress control. As shown in Fig. 2, all stresses are zero except for one shear stress, in this case τ_{xz} . The shear stress–shear strain response is shown in Fig. 3(b). The curve does not pass the peak stress because the numerical simulations were run under force (or stress) control. The applied shear stresses produce volumetric changes, as shown by the Mohr's circle in the strain space of Fig. 3(a), which refers to the last loading point in Fig. 3(b).

The simple shear test is such that only a shear strain (γ_{xz}) is applied with all other strains equal to zero (Fig. 4). Because the specimen tries to expand vertically in the z -direction but is restrained by the supports, confining stresses develop in the vertical direction. Fig. 5(a) shows the Mohr's circle in the stress space for the last loading point. Fig. 5(b) shows the shear stress–shear strain response, which strain-hardens because of the increasing

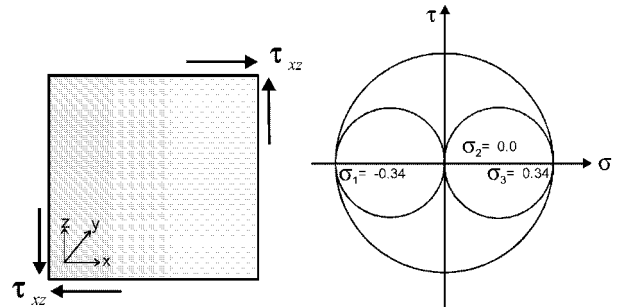


Fig. 2. Pure shear loading and Mohr's circle of stress.

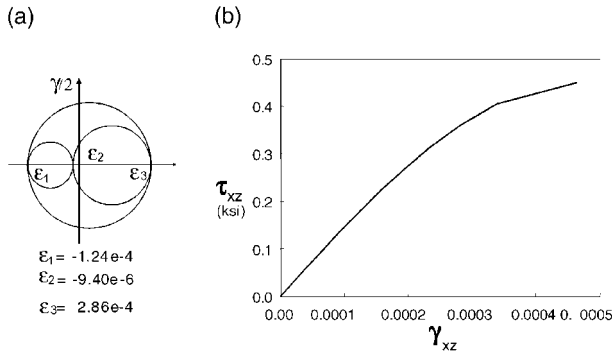


Fig. 3. Pure shear loading results (a) Mohr's circle of strain at last loading point; (b) stress-strain response.

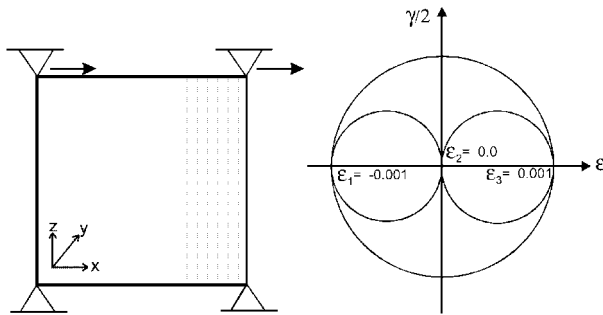


Fig. 4. Simple shear loading and Mohr's circle of strain.

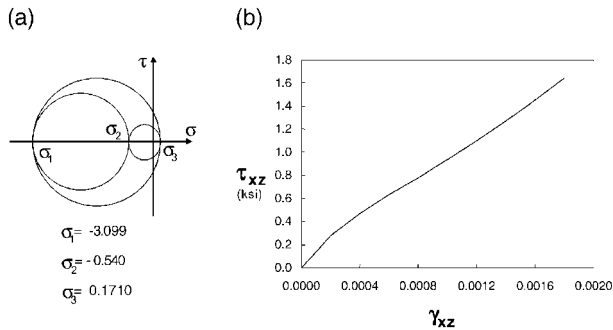


Fig. 5. Simple shear results (a) Mohr's circle of stress at last loading point; (b) stress-strain response.

confining stresses. Using the model originally developed by Balan et al. [2], the response of the simple shear test is similar to that of the pure shear test.

2.1.5. Crack model and concrete model implementation

Two major approaches exist to treat tensile cracking of concrete in FE analyses: discrete and smeared crack models. The discrete crack approach models cracks using interface elements between adjacent solid elements. While very precise, this approach requires a priori se-

lection of the crack orientation, or remeshing after the crack direction is detected. Multiple cracks or rotating cracks under non-proportional loads are also hard to model. The smeared crack approach assumes that the cracked solid is a continuum and the stress-strain relations of the integration points determine the orientation and the extension of the cracks. The above assumption does not match well the physical discontinuity of a crack. The controversy between the two approaches remains. The embedded crack model represents a good compromise between the two approaches, but the formulations proposed to date still have some severe problems [13].

The smeared crack approach is used in this study. It has been observed that the smeared crack model describes more realistically distributed crack patterns, such as those observed in structures with heavily distributed reinforcement. The smeared crack approach can however overestimate the shear stiffness of a structural element due to stress-locking in commonly used finite elements. The problem is typically avoided by using very refined meshes, which in turn increase the computational cost of the analyses. Smeared crack models use either fixed or rotating cracks. The fixed crack model was developed to include the advantages of the discrete crack approach into the smeared crack approach. The rotating crack allows the crack to rotate with the principal strain directions during loading. It was shown by Rots and Blaauwendraad [14] that the fixed smeared crack approach is more prone to stress-locking problems. Most of the rotating smeared crack models have coaxiality between principal stress and strain axes. However, it has been observed by Milford [15] that the principal stress directions do not coincide with the principal strain directions in a highly anisotropically reinforced section.

A rotating crack approach is used in the proposed model. The principal stress axes do not coincide with the principal strain axes. The concrete tensile response is assumed to be the reduced shape of the compression envelope curve with a fixed descending branch point defined as $f_t = 0.25f_c$ and $\epsilon_t = 3\epsilon_c$ (Fig. 1). The crack direction is assumed to be normal to the principal tensile strain directions.

The concrete model has been implemented in different solid elements in the finite element program FEAP [16]. Both a tangent and a total secant stiffness were used. The tangent method shows numerical difficulties around the peak of the stress-strain curve as the orthotropic moduli tend to zero. It was decided to use the total secant approach for the material driver, and either the initial stiffness or the total secant stiffness for the element. The implementation of the proposed model does not require iterations at the constitutive level and it shows a fast convergence even with the initial stiffness method. The flowchart of the concrete constitutive driver is illustrated in Fig. 6.

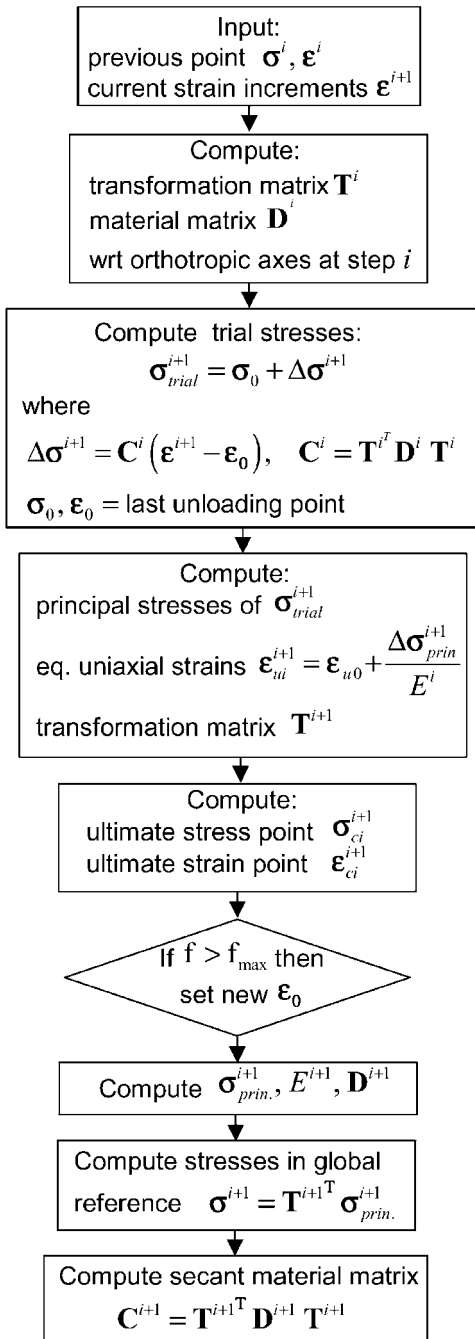


Fig. 6. Flow chart of constitutive driver for finite element implementation.

The concrete law is cyclic. The loading/unloading criterion is based on the loading function f defined as

$$f = \sqrt{\frac{\epsilon_{u1}^2 + \epsilon_{u2}^2 + \epsilon_{u3}^2}{\epsilon_{c1}^2 + \epsilon_{c2}^2 + \epsilon_{c3}^2}} \quad (12)$$

where ϵ_{ui} and ϵ_{ci} are the equivalent uniaxial strains and strains at peak stress, respectively. The loading and unloading conditions are:

$$\begin{aligned} f > f_{\max} & \text{ loading,} \\ f \leq f_{\max} & \text{ unloading} \end{aligned} \quad (13)$$

where f_{\max} is the maximum value of the loading function up to the current load step. Additional details on the cyclic rules are given in Refs. [2,5].

2.2. Reinforcing steel bar

A number of steel models have been proposed to simulate the response of steel structures. Some of these models are developed on the basis of material constitutive laws that rely on plasticity theory, particularly for solid elements. However, most of the uniaxial laws developed for the reinforcing steel bars are phenomenological models that simulate the response of the bars on the basis of experimental observations. In this study, a simple uniaxial, bi-linear, strain-hardening constitutive law is used.

3. Validation of concrete model

Several correlation studies with experimental results and parametric analyses were performed by Kwon [5] to validate the concrete constitutive law. Early results are reported in Ref. [2]. This paper presents two additional validation tests that deal with loading under different confinement conditions.

3.1. Constant confinement test

Fig. 7 compares the experimental and numerical responses of a specimen loaded in cyclic compression under a constant, lateral confinement pressure of 0.5 ksi. The test was performed by Hurlbut [17]. Partial unloading to specified strains was prescribed during the test. The unconfined compressive strength of the con-

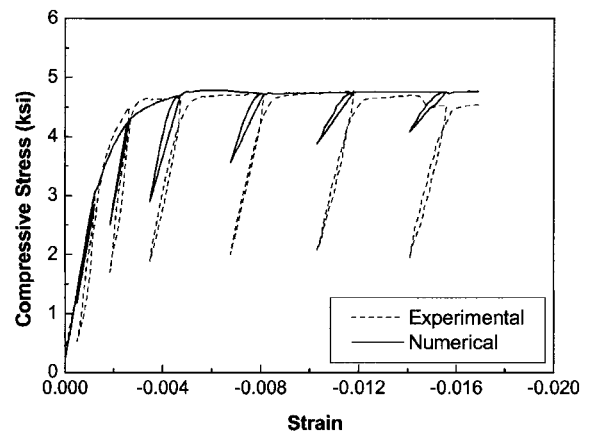


Fig. 7. Experimental [17] and numerical responses of concrete cylinder under constant confining stress of 0.5 ksi.

crete was 3.35 ksi. The numerical response shows an increase in compressive strength and matches very well the ductile response of the specimen. The unloading stiffness of the numerical results is smaller than that observed in the experimental results. The unloading rule of the uniaxial concrete curve of Fig. 1 points to a fixed, focal point. This stiffness degradation rule was derived from the work of Lee and Willam [24]. Additional cyclic tests are needed before more precise cyclic rules can be implemented. Stiffness and strength degradation under cyclic loads, as observed in experimental tests [25], is not considered in the model.

3.2. Steel vs FRP confined concrete

Steel and fiber reinforced polymer (FRP) jackets apply different confinement mechanisms to the concrete. The steel confinement increases initially as the compressive force on the concrete cylinder increases. After the steel jacket or the transverse reinforcement yields, the confining stress remains constant, and the results are similar to those obtained with constant confining pressure. The FRP jacket, on the other hand, remains basically elastic up to the point of failure, thus the confining pressure continuously increases with the applied compression force.

In order to study the two different confinement mechanisms, correlation studies with the experimental results of Orito et al. [18] and Mirmiran [19], as reported by Samaan et al. [20], are used. In both cases the specimens are circular cylinders. Both the steel and FRP jackets in circular specimens are modeled with four node axisymmetric elements. The steel law was an elastic–perfectly plastic model. The FRP jacket is made of unidirectional E glass fibers at $\pm 75^\circ$ windings, and is modeled as an isotropic, elastic–perfectly plastic material with a very short plastic region. The concrete and FRP material properties used in the experiments are given in Tables 1 and 2.

Both experimental and numerical results show that the confinement increases the strength of the specimen by a factor of three, as indicated in Figs. 8 and 9. The FRP confined specimen reaches almost the same compression strength as the steel-confined specimen with about half the thickness of the steel tube. The concrete

Table 1
Properties of concrete-filled steel and FRP tubes

Properties	Steel-confined concrete [18]	FRP-confined concrete [20]
Core diameter (in.)	4.50	5.71
Tube thickness (in.)	0.2	0.087
Unconfined concrete strength (ksi)	7.6	3.83

Table 2
Mechanical properties of E glass fibers and polyester resin in experiments by Samaan et al. [20]

Properties	450-yield E glass	Polyester resin
Tensile strength (ksi)	317	10.4
Tensile modulus (ksi)	10,100	630
Shear modulus (ksi)	4370	232
Poisson's ratio	0.22	0.36

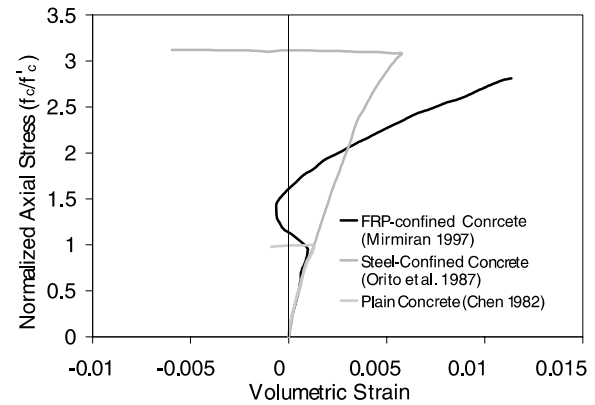


Fig. 8. Experimental volumetric strain response of concrete filled steel and FRP tubes [20].

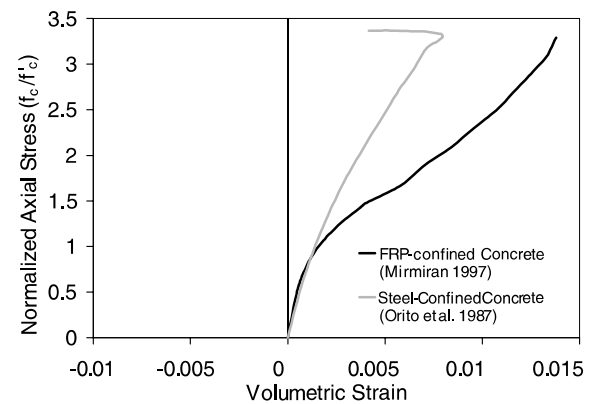


Fig. 9. Numerical volumetric strain response of concrete filled steel and FRP tubes.

filled steel tube exhibits an almost constant volume contraction up to the point where the jacket yields. After this point, the confining stress remains constant and the volume starts expanding. The numerical results are in very close agreement with the experimental tests, and were stopped earlier because of numerical problems when the Poisson's ratios approach the incompressible value. In the experimental response of the FRP filled tube, the volume initially contracts and then suddenly

changes tendency and increases, near the point of unconfined compressive strength, where larger cracks form in the specimen. This is due the fact that the FRP jacket was not engaged in the early stages of loading, because the concrete loosely filled the tube and because initially the fibers may be not perfectly aligned. Up to the point of unconfined compressive strength, the response is that of the unconfined cylinder. Only when the specimen approached and passed the unconfined compressive stress the cracks became larger, the volume started increasing, the jacket became engaged and the tendency was reversed, eventually showing volume contraction. The numerical simulations follow the same trend, but the FRP is engaged from the very beginning, therefore volumetric contraction is observed throughout the simulation. The compressive stress and the volumetric strain at which the FRP jacket fails correspond to the experimentally observed values.

Samaan et al. [20] define and study the dilation rate μ , which measures the rate of change of the radial strains ϵ_r in terms of the axial strain ϵ_c and is defined as:

$$\mu = -\frac{d\epsilon_r}{d\epsilon_c} \quad (14)$$

Fig. 10 shows the dilation-rate curve of concrete for the experimental results, as reported by Samaan et al. [20]. The dilation rate of the concrete filled steel tube is almost constant until the steel tube yields at an axial strain of approximately 0.01 and then increases almost linearly. For the concrete filled FRP tube Fig. 10 confirms that the jacket is not engaged initially, since the response is very close to that of the plain concrete specimen. The tendency is however totally reversed when the jacket is engaged and the dilation ratio decreases to the asymptotic value of approximately 0.3. The numerical results of Fig. 11 show good agreement in both cases, but, as mentioned earlier, they do not show the initial transition phase of the concrete filled FRP tube.

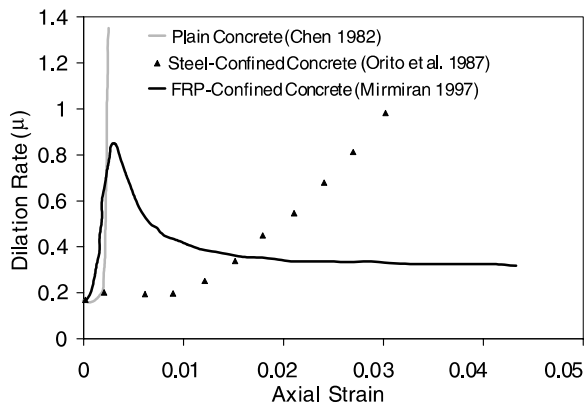


Fig. 10. Experimental dilation strain response of concrete filled steel and FRP tubes [20].

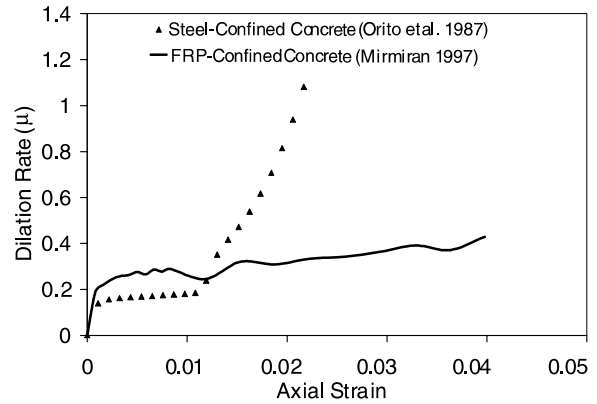


Fig. 11. Numerical dilation strain response of concrete filled steel and FRP tubes.

To further validate the concrete model developed in this study, additional correlation studies were performed using the experimental results reported by Mirmiran [19] on concrete cylinders confined by variable thickness FRP wraps: 6, 10, and 14 plies were used. The material properties of the glass FRP are shown in Table 3. The experimentally obtained unconfined concrete strength values did not correspond to the concrete strength in the wrapped specimen. Mirmiran [19] observed that because of the wraps, the concrete in the specimens was not totally hydrated at failure, thus the core concrete strength was not fully developed at the time of the experiments. To find the concrete strength at the time of the tests, Mirmiran [19] suggested to compute the concrete uniaxial strength f'_c from the measured concrete stiffness using the formula $E = 47586\sqrt{f'_c}$ suggested by Ahmad and Shah [21]. The original strengths and the re-computed values of each test are presented in Table 4.

Table 3
Mechanical properties of FRP tubes [19]

Specimen (plies FRP)	FRP strength (ksi)	FRP elastic modulus (ksi)
6	76	5400
10	84	5850
14	93	5910

Table 4
Unconfined concrete strength [19]

Specimen (plies FRP)	Concrete strength (ksi)	Recomputed strength (ksi)
6	4.299	5.393
10	4.476	2.137
14	4.299	3.551

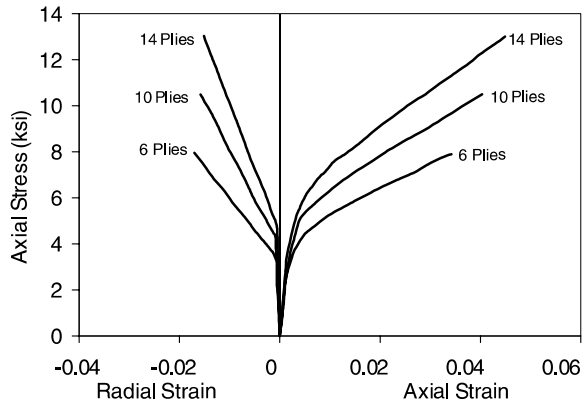


Fig. 12. Experimental response of concrete cylinders wrapped with FRP [20].

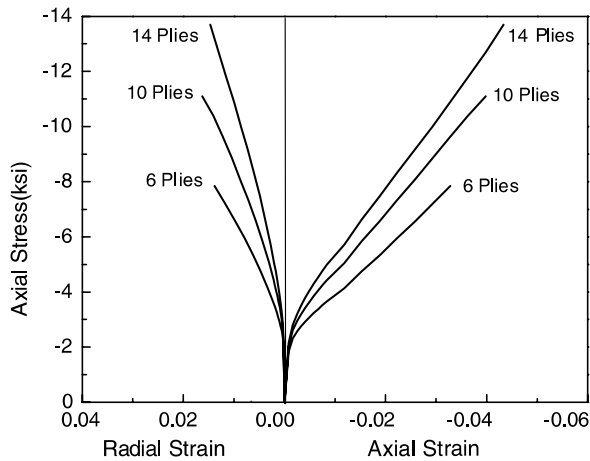


Fig. 13. Numerical response of concrete cylinders wrapped with FRP.

As shown in Figs. 12 and 13, the numerical results show good agreement with the experiments, both in terms of the radial and axial strains and in the prediction of the axial stress at failure. Fig. 12 contains the experimental results reported in Ref. [20]. The dots refer to their experimental results, while the solid lines refer to the predictions obtained with the confinement model proposed by Samaan et al. [20]. Fig. 13 contains the numerical results obtained with the model described in this paper. For the results of Fig. 13, the predicted peak strength is 2% higher than that of the experiments for 6 and 10 ply wraps, and 7% higher for 14 ply wraps. In the numerical results of Fig. 13, the beginning of the bilinear response is slightly lower than the experimental results. This discrepancy is mainly due to the uncertainties in determining the material properties of the concrete inside the FRP tube that, as previously noted, showed a high moisture content after specimen failure. Failure in both the experiments and the numerical simulations was caused by sudden failure of the FRP jacket.

4. Analysis of reinforced concrete columns

Three RC columns originally tested at the University of California, San Diego by Xiao et al. [22] are studied to validate the concrete model and its FE implementation in predicting the response of structural members. The columns represent a one third size replica of actual bridge piers built in the mid 1960s. The columns were fixed at both ends, and were loaded under constant axial load and increasing lateral tip displacement.

4.1. Material properties, geometry and loading

The Concrete and steel material properties of the experiments are presented in Table 5. The geometry and reinforcing details are shown in Fig. 14. The columns are labeled R1, R3 and R5 in the original report by Xiao et al. [22]. Specimens R1 and R3 are 96 in. high, column R5 is 72 in. high. For the longitudinal reinforcement, grade 40 steel was used for column R1 and grade 60 steel was used for columns R3 and R5. For the transverse reinforcement, grade 50 steel was used in column R1, and grade 40 steel was used for columns R3 and R5. The Young's modulus of steel is 29,000 ksi. The initial Poisson's ratio of concrete is assumed to be $\nu_0 = 0.2$.

To simplify the analyses and to reduce the computational time, the FE mesh does not include the concrete cover and the reinforcement bars in the footing and loading arm. The hoops in the z-direction are lumped to follow the mesh discretization. However, the same volumes of longitudinal and transverse steel used in the experiments are used in the FE analyses. In the y-direction, the mesh of the 8-node brick elements is not subdivided, as shown in Fig. 14. Both the longitudinal and transverse reinforcement bars are modeled as bar elements with a uniaxial bilinear constitutive law. The concrete is modeled by 3D 8-node brick elements with a $2 \times 2 \times 2$ Gauss integration scheme. Perfect bond between steel and concrete is assumed. The footing and loading arm are discretized with very stiff, linear elastic blocks to simulate the non-perfect fixity of the experimental boundary conditions. It should be noted that the boundary conditions are not perfectly symmetric, as shown in Fig. 14. In the experimental tests, the columns

Table 5
Material properties of three columns [22]

Test unit	Concrete strength (ksi)	Longitudinal steel f_y (ksi)	Hoops f_y (ksi)
R1	5.50	46.0	52.3
R3	4.95	68.1	47.0
R5	4.75	68.1	47.0

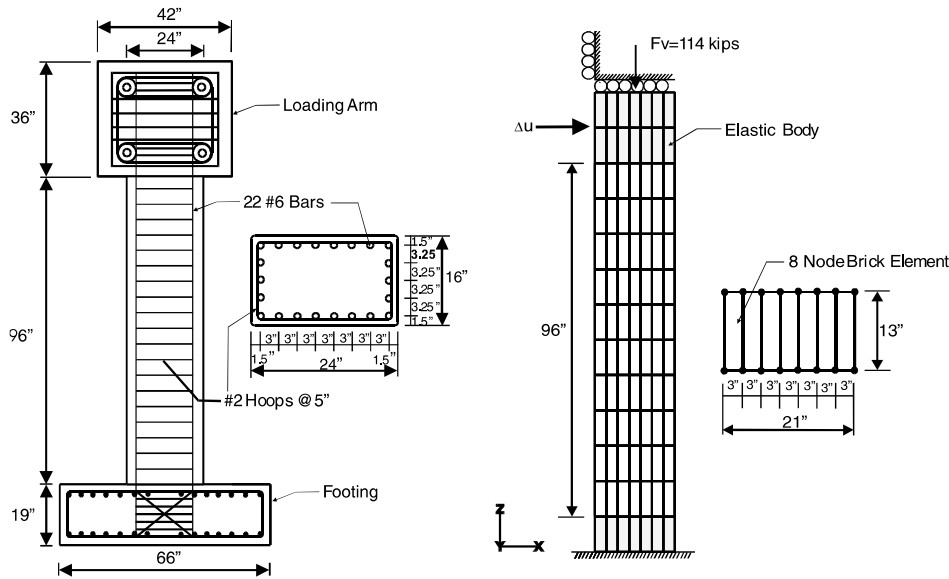


Fig. 14. Experimental setup, column details and finite element mesh for three columns tested at University of California at San Diego [22].

were subjected to a constant axial force of 114 kips and to lateral displacement cycles of increasing amplitude. Because of the computational cost of the analyses, which were performed on a 450 MHz Personal Computer, and because the failure mode of the three columns was the main focus of the study, only the monotonic loading envelope was followed in the numerical simulations.

4.2. Column R1

Unlike the other two columns, column R1 was designed not to be shear deficient. It has lower longitudinal steel strength and higher hoop strength (Table 5). Experimental and numerical results are shown in Fig. 15. Flexural-shear cracks were observed in the experiment, and the column strength dropped due to shear failure only in the very last cycles. The monotonic numerical results are in close agreement with the experimental ones. The small drop in the force–displacement curve is caused by the crushing failure of the compression strut that forms in the column (visible in Fig. 16, that shows the concrete vertical strain contours at a lateral displacement of 1.2 in.).

The tensile longitudinal reinforcing bars at the bottom and top section first reach the yield strains when the lateral force is equal to 95 kips (corresponding to a lateral displacement of 0.35 in.), close to the experimental observations that report that the longitudinal reinforcement first yielded at a lateral force of 90 kips and a lateral displacement of 0.32 in. Hoop yielding was not observed in the numerical results, even though the

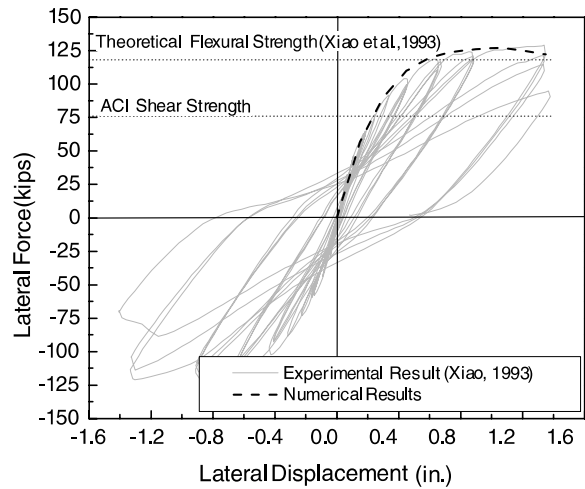


Fig. 15. Lateral force–displacement response of column R1.

lateral strain was very close to yielding at the end of analysis, while the hoop first yielded at a lateral displacement of 1.3 in. in the experiment.

4.2.1. Column R3

Column R3 has a lower concrete strength, larger longitudinal reinforcing bar strength and lower hoop strength than column R1 (Table 5). Column failure in the experiment followed the formation of major shear cracks, which resulted in a drastic loss of load carrying capacity, as shown in Fig. 17. Shear failure was reached before the flexural capacity of the column was attained.

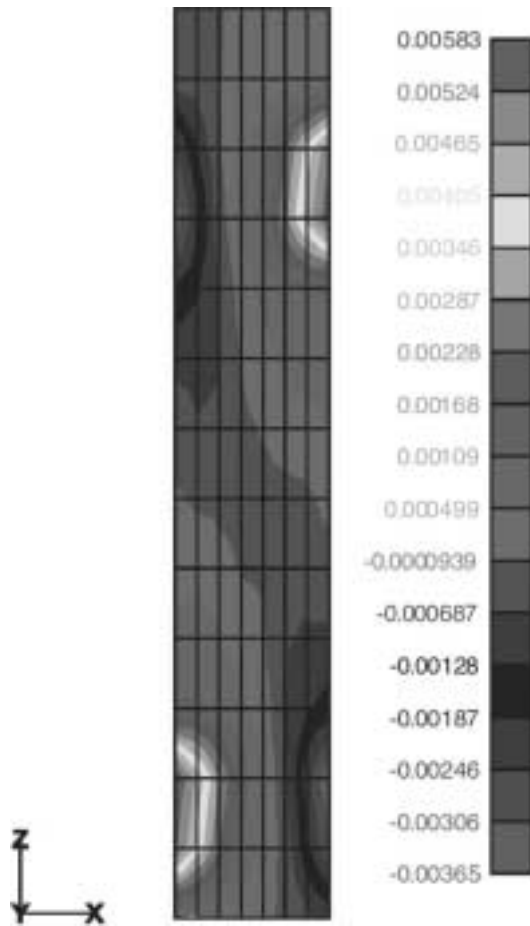


Fig. 16. Concrete ϵ_{zz} strain distribution in column R1 at a lateral displacement of 1.2 in.

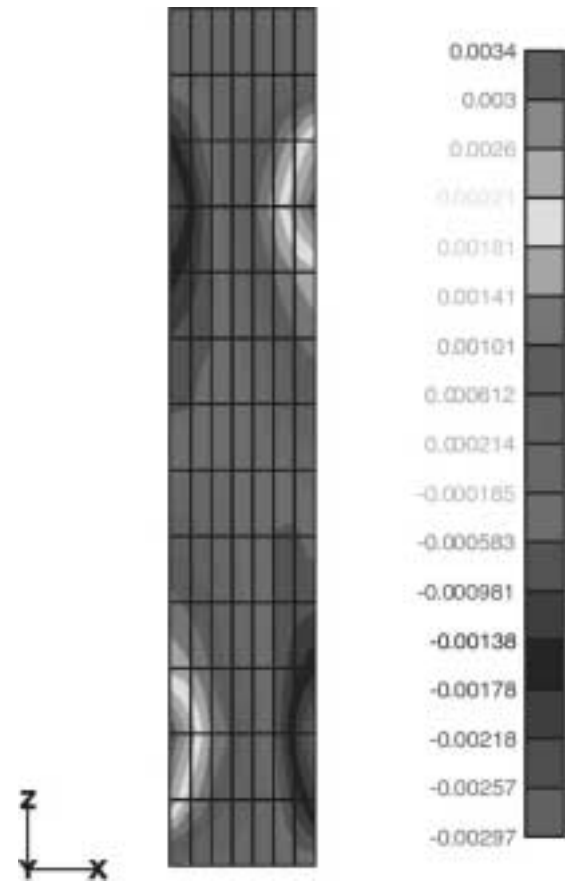


Fig. 18. Concrete ϵ_{zz} strain distribution in column R3 at a lateral displacement of 0.87 in.

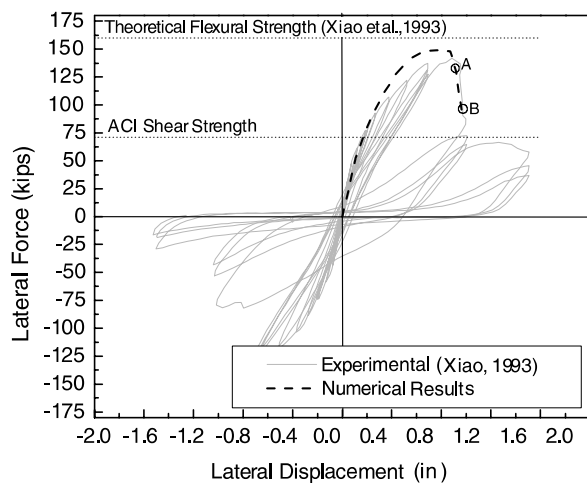


Fig. 17. Lateral force–displacement response of column R3.

The numerical results show a similar trend, but the drop in the column strength was initiated by crushing of the

concrete compression strut (visible in Fig. 18) at a lateral displacement of 0.87 in. (point A in Fig. 17), followed by sudden shear failure (points B in Fig. 17).

The lateral force level corresponding to the first yield of the longitudinal reinforcement is 120 kips in the experiment, at a lateral displacement is 0.52 in., and in the numerical results it is 133 kips at 0.547 in. In the experiment, the hoops at about 18 in. from the bottom first yielded at a lateral displacement of 0.79 in. The first hoop yielding of in the numerical results was observed at a lateral displacement of 0.919 in. near the middle of the column.

Fig. 19 illustrates more clearly the shear deformation and shear failure sequence of the column. Shear deformations in the experiment were measured at 32 in. intervals (one third of the column height). Because ten layers were used in the numerical analysis, the same intervals could not be matched. The shear deformations were averaged in the top and bottom three layers (28.8 in. high) and in the middle four layers (38.4 in. high). Even though the segment sizes in the experiment and in the numerical analysis are not identical, they are close

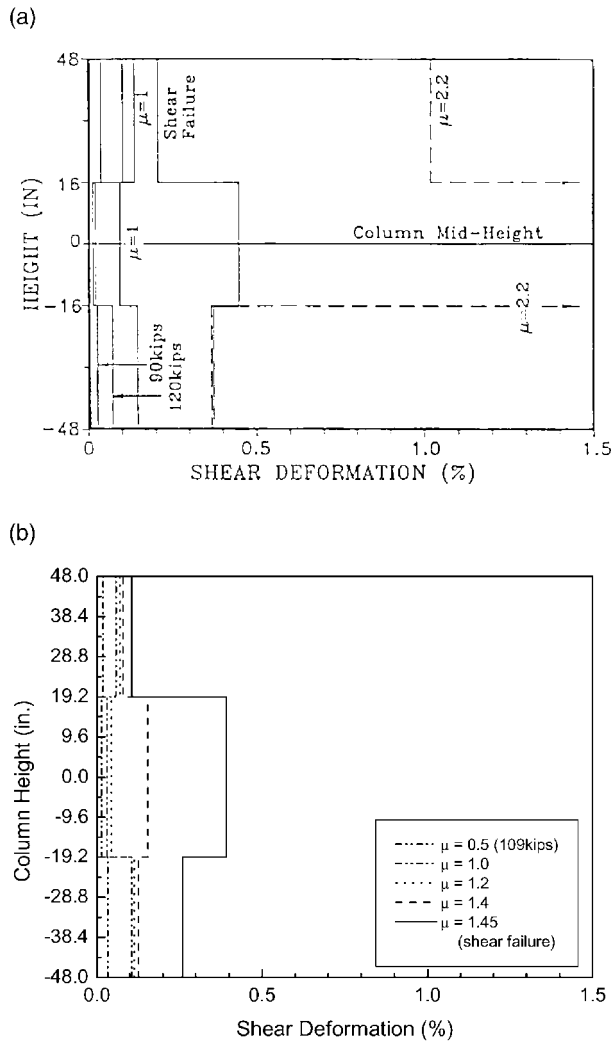


Fig. 19. Average shear strains in column R3 ($\mu = 1$ corresponds to a lateral displacement of 0.65 in. in Ref. [22]): (a) experimental results from Ref. [22] (shear failure at $\mu = 1.5$), (b) numerical results.

enough to compare the result trends. In the initial loading stages, the shear deformations are larger in the top and bottom thirds of the column. At larger displacements, a major shear crack forms in the mid third and the tendency inverts. This is shown in both the experimental and in the numerical results. It should also be noted that the large shear cracks in the mid third were accompanied by yielding of the hoops, which allows the crack to freely open. Shear failure took place at a ductility $\mu = 1.5$ in the experiment and $\mu = 1.45$ in the numerical simulation.

As previously pointed out, the lack of symmetry with respect to the column midheight in the numerical results derives from the fact that the end blocks do not apply perfectly symmetric boundary conditions (see mesh discretization in Fig. 14).

4.3. Column R5

Column R5 is shorter than the other columns and has a height-to-depth ratio equal to three. It has the lowest concrete strength of the three columns, while the steel properties are the same of column R3 (Table 5). Failure in the experiment was caused by the opening of large shear cracks, which lead to a sudden drop in the column strength (Fig. 20). Similarly to column R3, column R5 formed large shear cracks before the full flexural strength was reached. From Fig. 20 it appears that while the overall numerical curve is close to the experimental one, the numerical response is stiffer than the experimental one. This is due to a number of factors, such as the assumption of perfect bond between steel and concrete, and the use of the crude bilinear law for the steel reinforcement. In the numerical analysis, column failure is initiated by crushing of the compression strut (visible in Fig. 21) at a lateral displacement of approximately 0.5 in., followed by the opening of large shear cracks (point B in Fig. 20). Fig. 22 shows the shear distribution over the height of the column. In the experiment, the major shear cracks concentrate in the middle third of the column, while in the analysis the shear cracks start in the middle third and then extend to the bottom third of the column at a ductility of $\mu = 0.9$. Differences in the results may also be attributed to the difference in the sampling points between the tests and the numerical studies, as already commented for Fig. 19.

The first yield of the longitudinal reinforcement was observed at a lateral displacement of 0.51 in. in the experiment, and at a displacement of 0.403 in. the numerical simulations. The hoops did not yield in the numerical results (though they were close to the yield strain), while in the experiment some hoops first yielded at a lateral displacement of 0.42 in.

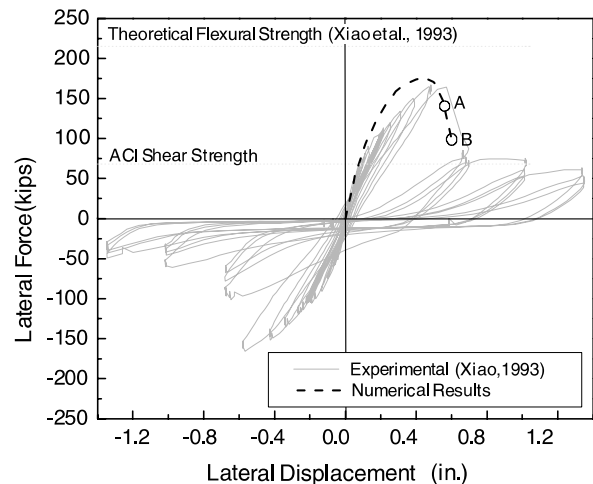


Fig. 20. Lateral force–displacement response of column R5.

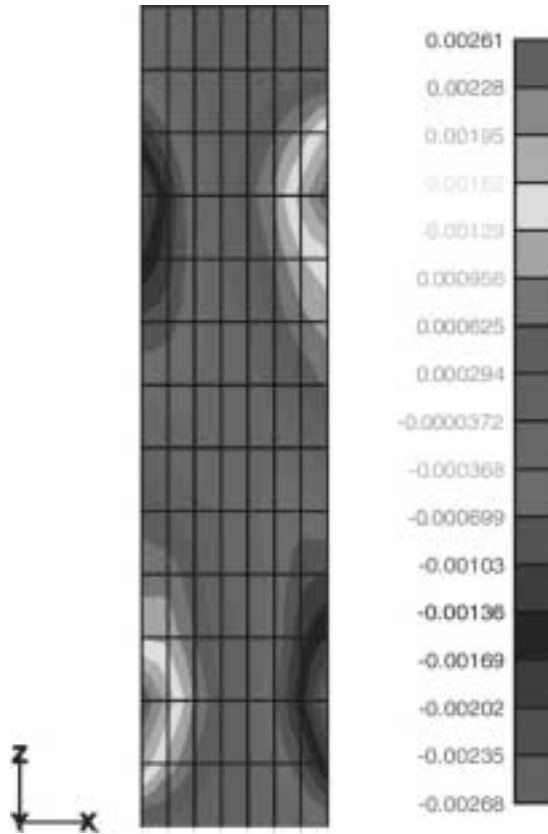


Fig. 21. Concrete ϵ_{zz} strain distribution in column R5 at a lateral displacement of 0.5 in.

5. Conclusions

A recently developed hypoelasticity-based concrete model is applied to the analysis of the three dimensional response of concrete specimens and RC columns. The concrete model is orthotropic, with the axes of orthotropy parallel to the principal stress directions. Principal stress and strain directions are not coaxial. The model is based on the concept of equivalent uniaxial strains first proposed by Darwin and Pecknold [4]. The original model by Balan et al. [2] is modified to include the coupling between the deviatoric and the volumetric stresses following the definition of a coupling modulus proposed by Gerstle [12]. The concrete model was implemented as a strain driven module in an existing FE program.

The validation studies presented in this paper focus on the shear response of the constitutive law and on the response of concrete specimens under different confinement mechanisms, mainly steel and FRP jackets. In all these validations tests the model closely traces the experimentally observed results.

The FE analyses of three RC columns tested at the University of California, San Diego [22] extend the concrete model application to the study of structural

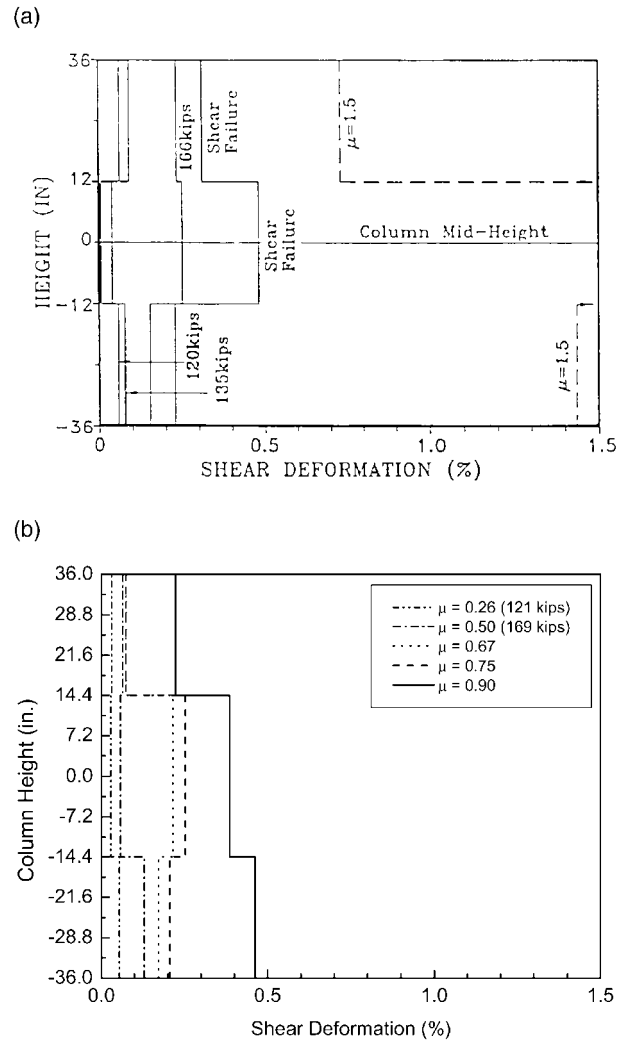


Fig. 22. Average shear strains in column R5 ($\mu = 1$ corresponds to lateral displacement of 0.67 in. in Ref. [22]): (a) experimental results from Ref. [22] (shear failure at $\mu = 1.0$), (b) numerical results.

members. In this case too, good agreement is observed between the specimen experimental and numerical results under a combination of lateral and axial loading. The yielding of the longitudinal reinforcing bar and the yielding of the shear reinforcement correlate well with the experimental results. Failure in the numerical analyses was initiated by crushing of the compressive strut, followed by the formation of large shear cracks. The simplicity of the constitutive model allowed the complex analyses of the three RC columns to be run economically. Also, structural failure of the columns was closely traced even for the shear deficient columns, where a sudden drop in load-carrying capacity is observed after the shear cracks open. The results of the analyses point to future enhancements of the numerical simulations, such as the inclusion of the bond-slip between the steel

rebars and the concrete, a more refined mesh and a better discretization of the footings and loading arm.

Acknowledgements

This work is partially supported by the National Science Foundation under grant no. CMS-9804613. This support is gratefully acknowledged. However, the opinions expressed in this paper are those of the writers and do not necessarily reflect those of the sponsor. Special thanks also go to Dr. T. Balan for his collaboration in the early stages of the concrete model development, and to Prof. K. Gerstle for his constructive comments and suggestions throughout this work.

References

- [1] Darwin D. Reinforced concrete. In: Finite element analysis of reinforced concrete II. American Society of Civil Engineers; 1993. p. 203–32.
- [2] Balan TA., Spacone E, Kwon M. A 3D hypoplastic model for cyclic analysis of concrete structures. *Eng Struct* 2001; 23(4):333–42.
- [3] Gerstle KH. Behavior of concrete under multiaxial stress states. *ASCE J Eng Mech* 1980;106(6):1383–403.
- [4] Darwin D, Pecknold DA. Nonlinear biaxial stress–strain law for concrete. *ASCE J Eng Mech* 1977;103(2):229–41.
- [5] Kwon M. Three dimensional finite element analysis of reinforced concrete members. PhD dissertation, Department of Civil, Environmental, and Architectural Engineering, University of Colorado, Boulder, 2000.
- [6] Popovics S. Numerical approach to the complete stress–strain relation for concrete. *Cement Concr Res* 1973;3(5): 583–99.
- [7] Saenz IP. Discussion of ‘Equation for the stress–strain curve of concrete’ by P. Desay and S. Krishnan. *ACI J* 1964;61(9):1229–35.
- [8] Willam KJ, Warnke EP. Constitutive models for the triaxial behavior of concrete. *Int Assoc Bridge Struct Proc* 1974; 19:1–30.
- [9] Menetrey P, Willam KJ. Triaxial failure criterion for concrete and its generalization. *ACI Struct J* 1995;92(3): 311–8.
- [10] Comité Euro-International du Béton. Concrete under multiaxial states of stress constitutive equations for practical design, *Bulletine d’Information* 156, 1983.
- [11] Smith SS, Willam KJ, Gerstle KH, Sture S. Concrete over the top, or: is there life after peak? *ACI J* 1989;86(5): 491–7.
- [12] Gerstle KH. Simple formulation of triaxial concrete behavior. *ACI J Proc* 1981;78(1):62–8.
- [13] Lotfi HR, Shing PB. Embedded representation of fracture in concrete with mixed finite elements. *Int J Numer Meth Eng* 1995;38:63–80.
- [14] Rots J, Blaauwendraad J. Crack models for concrete: discrete or smeared? fixed, multi-directional or rotating? Heron, Delft University of Technology, The Netherlands 1989;34(1).
- [15] Milford RV. The application of the rotating crack model to the analysis of reinforced concrete shells. *Comput Struct* 1985;20(1–3):225–34.
- [16] Taylor RL. FEAP User Manual v7.1. Department of Civil and Environmental Engineering, University of California, Berkeley, 1999. <http://www.ce.berkeley.edu/~rlt/feap/>.
- [17] Hurlbut BJ. Experimental and computational investigation of strain-softening in concrete. Report AFOSR 82-0273, CEAE Department, University of Colorado, Boulder, 1985.
- [18] Orito Y, Sato T, Tanaka N, Watanabe Y. Study on the unbounded steel tube structure. In: Proceedings of the International Conference of Composite Construction in Steel and Concrete. ASCE; 1987. p. 786–804.
- [19] Mirmiran A. Analytical and experimental investigation of reinforced concrete columns encased in fiberglass tubular jackets and use of fiber jacket for pile splicing. Final Report, contract no. B-9135. Florida Department of Transportation, Tallahassee, Florida, 1997.
- [20] Samaan M, Mirmiran A, Shahawy M. Model of concrete confined by fiber composites. *ASCE J Struct Eng* 1998; 124(9):1025–31.
- [21] Ahmad SH, Shah SP. Stress–strain curves of concrete confined by spiral reinforcement. *ASCE J Struct Eng* 1982;115(11):3036–54.
- [22] Xiao Y, Priestley MJN, Seible F. Steel jacket retrofit for enhancing shear strength of short rectangular reinforced concrete columns. Report No. SSRP-92/07, University of California, San Diego, 1993.
- [23] Lekhnitskii SG. In: Brandstatter JJ, editor. Theory of elasticity of an anisotropic elastic body. San Francisco, CA: Holden Day, Inc; 1963.
- [24] Lee Y-H, Willam KJ. Mechanical properties of concrete in uniaxial compression. *Am Concr Inst Mater J* 1997; 94(6):457–71.
- [25] Paskova T, Meyer C. Low-cycle fatigue of plain and fiber-reinforced concrete. *Am Concr Inst Mater J* 1997;94(4): 273–85.